

## ARTICLE OPEN



# Layer control of $\text{Sr}_{1.8}\text{Bi}_{0.2}\text{Na}_{n-3}\text{Nb}_n\text{O}_{3n+1}$ ( $n = 3-5$ ) perovskite nanosheets: dielectric to ferroelectric transition of film deposited by Langmuir Blodgett method

So-Yeon Yoo<sup>1,2,5</sup>, Haena Yim<sup>1,5</sup>, Ahrom Ryu<sup>1,2</sup>, Chansoo Yoon<sup>3</sup>, Bae Ho Park<sup>3</sup>, Sahn Nahm<sup>2</sup> and Ji-Won Choi<sup>1,4</sup>✉

Solution-based processable high- $k$  2-dimensional (2D) ferroelectrics have attracted significant interest for use in next-generation nanoelectronics. Although few studies on potential 2D ferroelectric nanosheets in local areas have been conducted, reports on the thin-film characteristics applicable to the device are insufficient. In this study, we successfully synthesize high- $k$  2D  $\text{Sr}_{1.8}\text{Bi}_{0.2}\text{Na}_{n-3}\text{Nb}_n\text{O}_{3n+1}$  (octahedral units,  $n = 3-5$ ) nanosheets by the engineering of the  $n$  of  $\text{NbO}_6$  octahedral layers with A-site modification, and realized ferroelectric characteristics in ultrathin films (below 10 nm). The nanosheets are synthesized by a solution-based cation exchange process and deposited using the Langmuir-Blodgett (LB) method. As increasing the  $\text{NbO}_6$  octahedral layer, the thickness of the nanosheets increased and the band gaps are tuned to 3.80 eV ( $n = 3$ ), 3.76 eV ( $n = 4$ ), and 3.70 eV ( $n = 5$ ). In addition, the dielectric permittivity of the 5-layer stacked nanofilm increase to 26 ( $n = 3$ ), 33 ( $n = 4$ ), and 62 ( $n = 5$ ). In particular, the increased perovskite layer exhibits large distortions due to the size mismatch of Sr/Bi/Na ions at the A-site and promotes local ferroelectric instability due to its spontaneous polarization along the  $c$ -axis caused by an odd  $n$  number. We investigate the stable ferroelectricity in Pt/ 5-layer  $\text{Sr}_{1.8}\text{Bi}_{0.2}\text{Na}_2\text{Nb}_5\text{O}_{16}$  / Nb:STO capacitor by polarization-electric field (P-E) hysteresis; the coercive electric field ( $E_c$ ) was 338 kV  $\text{cm}^{-1}$  and the remnant polarization ( $P_r$ ) 2.36  $\mu\text{C cm}^{-2}$ . The ferroelectric properties of ultrathin 2D materials could drive interesting innovations in next-generation electronics.

npj 2D Materials and Applications (2023)7:53; <https://doi.org/10.1038/s41699-023-00418-9>

## INTRODUCTION

Over the last decade, nanoelectronic devices based on 2-dimensional (2D) materials have become an emerging platform for overcoming the limitations of the continuous scaling down of conventional electronic devices<sup>1,2</sup>. Among the various strategies for investigating 2D materials, a solution-based liquid-phase exfoliation process has been considered a promising route for industrial-scale mass production and enablement for application in next-generation flexible electronics<sup>3-5</sup>. In particular, layered perovskite structure materials have strong in-plane covalent or ionic bonding within the layer and weak van der Waals bonding at the interlayer; therefore, these compounds can be easily exfoliated by simple cation exchange reactions. Moreover, its properties can be tuned using an exchangeable interlayer metal cation. Therefore, they have received considerable attention owing to their diverse properties, such as ferroelectric<sup>6</sup>, dielectric<sup>7</sup>, magnetic<sup>8</sup>, and photocatalytic activities<sup>9</sup>.

Layered perovskites consist of three different structures: Dion-Jacobson (DJ) with the structure of  $A'[\text{A}_{n-1}\text{B}_n\text{O}_{3n+1}]$ , Ruddlesden-Popper (RP) with the structure of  $A'_2[\text{A}_{n-1}\text{B}_n\text{O}_{3n+1}]$ , and Aurivillius (AU) with the structure of  $\text{Bi}_2\text{O}_2[\text{A}_{n-1}\text{B}_n\text{O}_{3n+1}]$ , where  $A'$  = alkali metal,  $A$  = rare earth, alkaline-earth, alkali metal,  $B$  = transition metal, and  $n$  = number of perovskite layers. Among them, DJ-phase compounds incorporating  $d^0$  cations such as  $\text{Nb}^{5+}$  and  $\text{Ta}^{5+}$  are wide-bandgap semiconductors or insulators, so they can be utilized as high- $k$  dielectrics<sup>10</sup>. Moreover, their characteristics can be easily tuned by controlling the composition of the  $[\text{A}_{n-1}\text{B}_n\text{O}_{3n+1}]$  layers and the number of octahedral units ( $n$ ).

For example, the dielectric permittivity of  $\text{Ca}_2\text{Nb}_3\text{O}_{10}$  can be improved by A-site modification with Sr ions, which have a higher polarizability. In addition, the leakage current density can be improved by B-site modification with Ta ions, which are less electronegative<sup>11,12</sup>. In addition, Li et al. successfully demonstrated the ferroelectric behavior of  $\text{Ca}_2\text{Na}_2\text{Nb}_5\text{O}_{16}$  nanosheet flakes through piezoelectric force microscopy (PFM) experiments by increasing the number of perovskite layers of  $\text{Ca}_2\text{Nb}_3\text{O}_{10}$ . The increased  $\text{NbO}_6$  unit cell promoted local ferroelectric instability and caused large distortions in the  $[\text{A}_{n-1}\text{B}_n\text{O}_{3n+1}]$  perovskite layer, thereby implementing ferroelectric properties<sup>13</sup>. With the discovery of these 2D oxide ferroelectrics, it is expected that the possibility of developing 2D stacked ferroelectric devices that show low energy consumption and high operating speed is approaching<sup>14</sup>. The thickness of these exfoliated nanosheets is only  $\sim 1$  nm; therefore, it is possible to design new building blocks using various neatly packed nanosheets. However, to stack the 2D nanosheet ferroelectric thin film with other 2D materials such as  $\text{MoS}_2$  channels to become electronic devices, it is necessary to verify characteristics such as P-E hysteresis of a large area rather than nanoscale characteristics such as PFM. In addition, only a few studies on liquid-exfoliated 2D ferroelectric oxides, including  $\text{Ca}_2\text{Na}_2\text{Nb}_5\text{O}_{16}$  and  $\text{ZnO}$ , have been reported<sup>13,15</sup>.

In this study, we propose a strategy to obtain 2D  $\text{Sr}_{1.8}\text{Bi}_{0.2}\text{Na}_{n-3}\text{Nb}_n\text{O}_{3n+1}$  (octahedral units,  $n = 3-5$ ) dielectric and ferroelectric nanosheets by simultaneously applying A-site substitution by increasing the number of  $\text{NbO}_6$  octahedra. We previously reported Bi-substituted  $\text{Sr}_2\text{Nb}_3\text{O}_{10}$ ,  $\text{Sr}_{1.8}\text{Bi}_{0.2}\text{Nb}_3\text{O}_{10}$

<sup>1</sup>Electronic Materials Research Center, Korea Institute of Science and Technology, Seoul 02792, Republic of Korea. <sup>2</sup>Department of Material Science and Engineering, Korea University, Seoul 02841, Republic of Korea. <sup>3</sup>Division of Quantum Phases & Devices, Department of Physics, Konkuk University, Seoul 05029, Republic of Korea. <sup>4</sup>Division of Nanoscience & Technology, KIST School, University of Science and Technology, Seoul 02792, Republic of Korea. <sup>5</sup>These authors contributed equally: So-Yeon Yoo, Haena Yim. ✉email: jwchoi@kist.re.kr

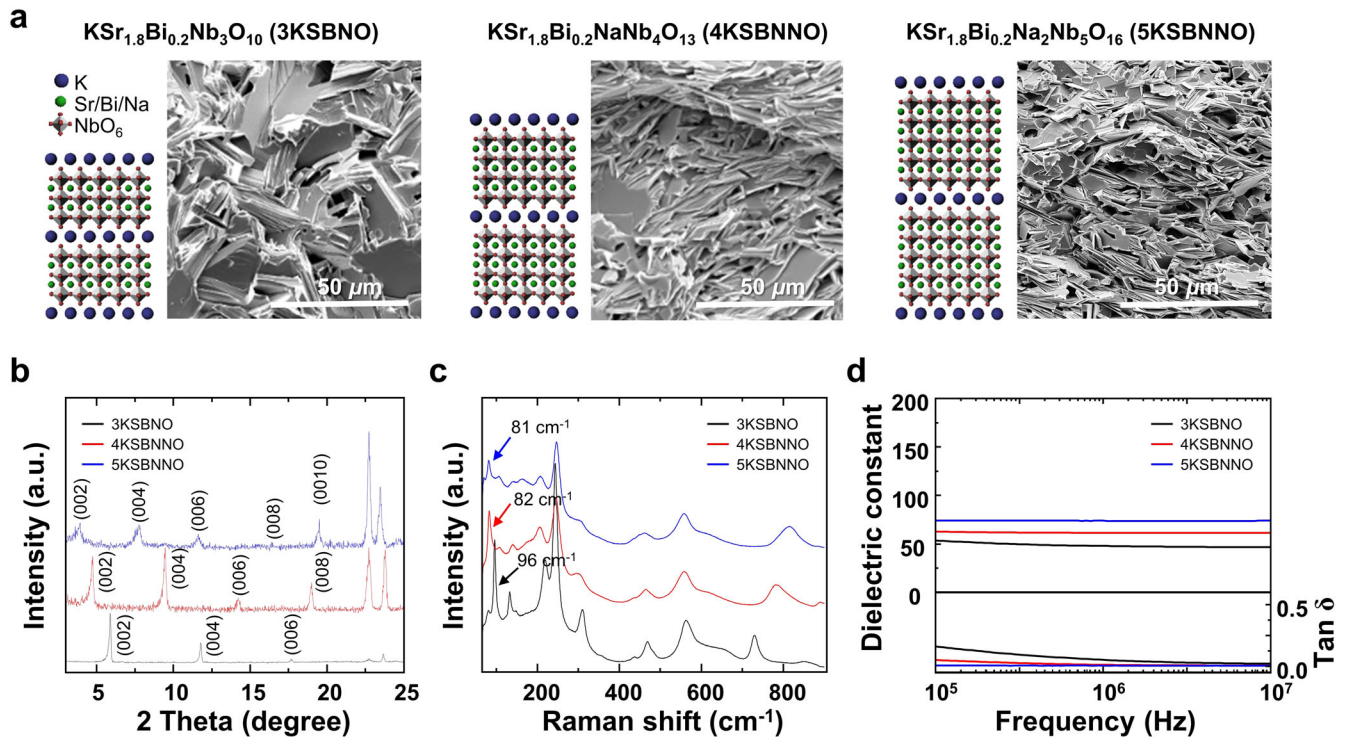


**Fig. 1** Structural analysis and dielectric properties of the composition of  $n$ KSBNNO ( $n = 3-5$ ). **a** Schematic diagram and SEM image of  $\text{KSr}_{1.8}\text{Bi}_{0.2}\text{Na}_{n-3}\text{Nb}_n\text{O}_{3n+1}$  ( $n = 3-5$ ) ( $n$ KSBNNO,  $n =$  number of  $\text{NbO}_6$  layer) sintered at  $1250^\circ\text{C}$ . **b** XRD patterns of sintered  $n$ KSBNNO. **c** Raman Spectra of  $n$ KSBNNO. **d** Dielectric constant and dielectric loss of  $n$ KSBNNO according to the frequency.

(polarizability of  $\text{Bi}^{3+} = 6.12 \text{ \AA}$  and  $\text{Sr}^{2+} = 4.24 \text{ \AA}$ ) nanosheets, which exhibit high dielectric permittivity due to high-valent and more polarizable Bi ions in the perovskite lattice<sup>16</sup>. To identify the optimal  $\text{Bi}^{3+}$  substitution level, the chemical formula of  $\text{KSr}_{2(1-x)}\text{Bi}_{2x}\text{Nb}_3\text{O}_{10}$  was varied by changing the value of  $x$  from  $x = 0.1$  to  $x = 0.3$ . Subsequently, we focused our research on the composition with  $x = 0.1$ , which exhibited excellent solution stability and high film yield after performing a soft chemical method. To induce ferroelectric characteristics while maintaining a high- $k$  dielectric in the  $\text{Sr}_{1.8}\text{Bi}_{0.2}\text{Nb}_3\text{O}_{10}$  nanosheet, we controlled the number of  $\text{NbO}_6$  unit cells of  $\text{Sr}_{1.8}\text{Bi}_{0.2}\text{Nb}_3\text{O}_{10}$  nanosheets by introducing  $\text{NaNbO}_3$  into  $\text{KSr}_{1.8}\text{Bi}_{0.2}\text{Nb}_3\text{O}_{10}$  parent material.  $\text{KSr}_{1.8}\text{Bi}_{0.2}\text{Na}_{n-3}\text{Nb}_n\text{O}_{3n+1}$  ( $n = 3-5$ ) was synthesized via a solid-state reaction, and each perovskite layer was exfoliated using a soft chemical method. There are various methods available for depositing nanosheets, such as spin-coating<sup>17</sup>, layer-by-layer<sup>18</sup>, Electrophoretic deposition (EPD)<sup>19</sup> and Langmuir-Blodgett (LB) deposition<sup>7</sup>. LB deposition enables facile and precise control of film thickness with no dead layer<sup>20</sup>. Thus, the successfully synthesized nanosheets were deposited on a Si wafer substrate using LB deposition.

We explored the dielectric properties and P-E hysteresis loops of  $\text{Sr}_{1.8}\text{Bi}_{0.2}\text{Na}_{n-3}\text{Nb}_n\text{O}_{3n+1}$  ( $n = 3-5$ ) nanosheet thin films according to their frequency. Consequently, we obtained ferroelectric characteristics in  $\text{Sr}_{1.8}\text{Bi}_{0.2}\text{Na}_2\text{Nb}_5\text{O}_{16}$  thin films, which shows higher polarizability and local ferroelectric instability due to increased  $\text{NbO}_6$  octahedra in the lattices.

## RESULTS AND DISCUSSION

### Structural and dielectric properties of $n$ KSBNNO ( $n = 3-5$ )

$\text{KSr}_{1.8}\text{Bi}_{0.2}\text{Na}_{n-3}\text{Nb}_n\text{O}_{3n+1}$  ( $n = 3-5$ ) ceramics were synthesized by a conventional solid-state reaction and the SEM images of the ceramics with structural schematic diagrams are presented in Fig. 1a. The structure of  $\text{KSr}_{1.8}\text{Bi}_{0.2}\text{Na}_{n-3}\text{Nb}_n\text{O}_{3n+1}$  ( $n = 3-5$ ) contains an edge-shared  $\text{NbO}_6$  octahedra with large cations occupying 12

coordinates located at the center of each cube, as seen in the conventional perovskite structure<sup>21</sup>. As shown in the schematic diagrams, the  $\text{K}^+$  layer and  $(\text{Sr}_{1.8}\text{Bi}_{0.2}\text{Na}_{n-3}\text{Nb}_n\text{O}_{3n+1})^-$  perovskite layers were repeatedly stacked. All the samples have sufficient particle sizes to be exfoliated and compact plate-like lamellar structure shown as SEM images in Fig. 1a. As shown in Fig. 1b, XRD analysis shows the x-ray patterns of  $\text{KSr}_{1.8}\text{Bi}_{0.2}\text{Na}_{n-3}\text{Nb}_n\text{O}_{3n+1}$  ( $n = 3-5$ ) and all peaks are well indexed with the Dion-Jacobson structure layered perovskite material. As increased the number of perovskite unit cells ( $n$ ), the (00 $l$ ) peaks gradually appeared and shifted to lower angle. This indicates that the thickness of the perovskite layers increased with the addition of the  $\text{NbO}_6$  layer<sup>22</sup>.

Figure 1c shows the Raman spectrum of  $\text{KSr}_{1.8}\text{Bi}_{0.2}\text{Na}_{n-3}\text{Nb}_n\text{O}_{3n+1}$  ( $n = 3-5$ ) at room temperature in the wavenumber range of  $50-1100 \text{ cm}^{-1}$ . The Raman band peaks between  $800$  and  $900 \text{ cm}^{-1}$  indicate a highly distorted  $\text{NbO}_6$  octahedra at the layer boundary assigned to the vibrational mode. In addition, the stretching of the internal and slightly distorted  $\text{NbO}_6$  octahedra band peaks were observed between the  $400$  and  $800 \text{ cm}^{-1}$  bands. The vibration and bending modes of the  $\text{NbO}_6$  octahedra are related to the  $200-450 \text{ cm}^{-1}$  band. A low phonon energy transition band exists below  $200 \text{ cm}^{-1}$ <sup>23</sup>. A gradual shift of the Raman band from  $\sim 730$  to  $\sim 810 \text{ cm}^{-1}$  presents that the number of  $\text{NbO}_6$  octahedral layers increased from three to five<sup>24</sup>. It is known that the behavior of the lowest-frequency mode is most affected by dielectric characteristics because the polarizability of perovskite materials is characterized by a delicate balance between the ionic bonding and covalent bonding between the metal ions and oxygen atoms in the  $\text{NbO}_6$  octahedra<sup>22</sup>. In the case of the  $\text{KSr}_{1.8}\text{Bi}_{0.2}\text{Na}_{n-3}\text{Nb}_n\text{O}_{3n+1}$  ( $n = 3-5$ ) ceramics, the intercalated  $\text{K}^+$  layers separate  $(\text{Sr}_{1.8}\text{Bi}_{0.2}\text{Na}_{n-3}\text{Nb}_n\text{O}_{3n+1})^-$  layers. Therefore, as the octahedral units ( $n$ ) decrease, the Nb-O-Nb chain is divided into smaller units, which affects the frequency of the phonon mode to a higher energy, hardening the soft-mode vibrations, and decreasing the overall dielectric

permittivity<sup>22,25</sup>. The Raman spectra in the low-frequency band shifted from 96 to 81  $\text{cm}^{-1}$  with increasing  $\text{NbO}_6$  octahedra (96  $\text{cm}^{-1}$  for  $n=3$ , 82  $\text{cm}^{-1}$  for  $n=4$ , and 81  $\text{cm}^{-1}$  for  $n=3$ ). These results were expected to exhibit improved dielectric properties when  $n=5$ .

The dielectric properties at 10 kHz to  $\sim 10$  MHz of  $\text{KSr}_{1.8}\text{Bi}_{0.2}\text{Na}_{n-3}\text{Nb}_n\text{O}_{3n+1}$  ( $n=3-5$ ) pellets are shown in Fig. 1d. As expected, the dielectric permittivity increased in proportion to the  $n$  value because the dipole moment of the specimen increased as the number of  $\text{NbO}_6$  octahedral layers between the  $\text{K}^+$  layers<sup>22,25</sup>. Increased octahedral layers lead to higher polarizability and enhanced dielectric permittivity, as indicated by the lowest-frequency mode of the Raman data. These phenomena can also be found not only in the same DJ structure but also in the AU and RP structures<sup>26,27</sup>. In addition, the distortion, which enhances the dielectric permittivity, may increase owing to the increasing number of Sr, Bi, and Na cations located at the A site as the  $n$  value increases<sup>16</sup>.

### Structural properties of $n$ SBNNO ( $n=3-5$ ) nanosheets

After investigating the bulk properties,  $\text{Sr}_{1.8}\text{Bi}_{0.2}\text{Na}_{n-3}\text{Nb}_n\text{O}_{3n+1}$  ( $n=3-5$ ) nanosheets were obtained by a 2-step cation exchange process using  $\text{KSr}_{1.8}\text{Bi}_{0.2}\text{Na}_{n-3}\text{Nb}_n\text{O}_{3n+1}$  ( $n=3-5$ ) sintered materials, as shown in Fig. 2a  $\text{K}^+$  ions were exchanged for the  $\text{H}^+$  and  $\text{TBA}^+$  layers. Bulky  $\text{TBA}^+$  ions were intercalated between the perovskite layers, and each layer was naturally exfoliated. The XRD and SEM results before and after acid substitution of  $\text{HSr}_{1.8}\text{Bi}_{0.2}\text{Na}_{n-3}\text{Nb}_n\text{O}_{3n+1}$  ( $n=3-5$ ) are shown in Supplementary Figure 1. K form powder is converted into H form powder through acid exchange, leading to swelling due to the difference in ion sizes. The increased interlayer distance in the perovskite structure can be observed by the XRD peaks shifting to lower angles as

shown in Supplementary Figure 1a ~ c. SEM analysis confirms the well-preserved layered structure at the edges of the fully acid-exchanged H form powder as indicated in Supplementary Figure 1d ~ f. It can be seen that there was no change in the structure arising from the acid exchange process. The stability of the colloidal suspension after the  $\text{TBA}^+$  exchange process was investigated using the Tyndall effect and zeta potential, as shown in Supplementary Figure 2. The clear Tyndall effect images confirm the presence of a large amount of dispersed nanosheets in the solution and their stable colloidal nature<sup>28</sup>. The zeta potentials of the  $\text{Sr}_{1.8}\text{Bi}_{0.2}\text{Na}_{n-3}\text{Nb}_n\text{O}_{3n+1}$  ( $n=3-5$ ) were measured as  $-38.81$  mV ( $n=3$ ),  $-37.33$  mV ( $n=4$ ), and  $-36.06$  mV ( $n=5$ ), and the absolute value of zeta potential beyond 30 mV is generally well known as stable colloidal suspension<sup>29</sup>.

Figure 2b shows a schematic diagram of the unit cell of the  $\text{Sr}_{1.8}\text{Bi}_{0.2}\text{Na}_{n-3}\text{Nb}_n\text{O}_{3n+1}$  ( $n=3-5$ ) nanosheets with AFM images. The thickness of  $\text{Sr}_{1.8}\text{Bi}_{0.2}\text{Nb}_3\text{O}_{10}$ ,  $\text{Sr}_{1.8}\text{Bi}_{0.2}\text{NaNb}_4\text{O}_{13}$ , and  $\text{Sr}_{1.8}\text{Bi}_{0.2}\text{Na}_2\text{Nb}_5\text{O}_{16}$  nanosheets is 1.8 nm, 2.2 nm, and 2.6 nm, respectively. As the number of octahedral units ( $n$ ) increased, the thickness also increased by 0.4 nm, indicating the addition of one  $\text{NbO}_6$  octahedra<sup>30</sup>. This value is slightly larger than the crystallographic thickness ( $\text{Sr}_2\text{Nb}_3\text{O}_{10} = 1.44$  nm), but it is due to the adsorption of residual molecules such as water or organic molecules on the nanosheet surface<sup>31,32</sup>. Additionally, the lateral size of nanosheets can also be confirmed in Fig. 2b. After the exfoliation process, the lateral size of nanosheets is reduced to a few micrometers due to the mechanical shaking for well dispersion in colloidal solution. UV-visible measurements of the  $\text{Sr}_{1.8}\text{Bi}_{0.2}\text{Na}_{n-3}\text{Nb}_n\text{O}_{3n+1}$  ( $n=3-5$ ) nanosheet solution are shown in Fig. 2c. The spectrum for all nanosheet solutions exhibited broad absorption below 300 nm. The indirect bandgap can be identified from the UV-vis analysis using the Tauc plot formula:  $(\alpha h\nu)^{1/2}$ , where  $\alpha$  is the absorption

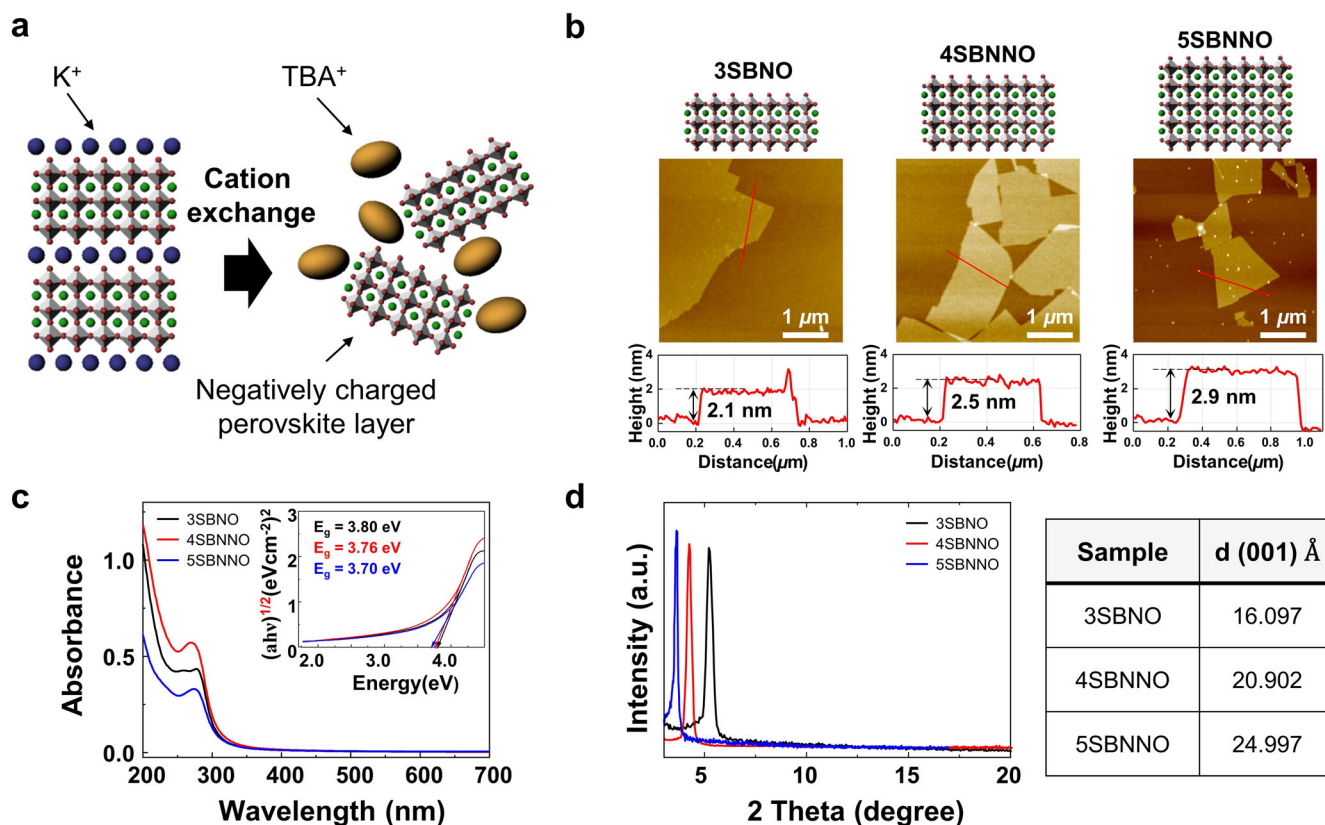


**Fig. 2** Structural and morphological analysis of  $n$ SBNNO ( $n=3-5$ ) nanosheets. **a** Schematic diagram of the cation exchange process. **b** Schematic diagram of the thickness controlled  $\text{Sr}_{1.8}\text{Bi}_{0.2}\text{Na}_{n-3}\text{Nb}_n\text{O}_{3n+1}$  ( $n=3-5$ ) ( $n$ SBNNO,  $n$  number of  $\text{NbO}_6$  layer) perovskite nanosheets with its AFM images. **c** UV-vis Optical absorbance and Tauc-plot of  $n$ SBNNO. **d** XRD pattern of 5-layer stacked  $n$ SBNNO nanosheets films.

coefficient and  $h\nu$  is the energy of the light. The calculated band gaps of  $\text{Sr}_{1.8}\text{Bi}_{0.2}\text{Nb}_3\text{O}_{10}$ ,  $\text{Sr}_{1.8}\text{Bi}_{0.2}\text{NaNb}_4\text{O}_{13}$ , and  $\text{Sr}_{1.8}\text{Bi}_{0.2}\text{Na}_2\text{Nb}_5\text{O}_{16}$  are 3.80 eV, 3.76 eV, and 3.70 eV, respectively (Fig. 2c inset). As a result, we confirmed that the bandgap energy decreased as the number of  $\text{NbO}_6$  layers increased because of the reduced quantum confinement owing to the broadening of the electronic band<sup>33</sup>.

These three types of  $\text{Sr}_{1.8}\text{Bi}_{0.2}\text{Na}_{n-3}\text{Nb}_n\text{O}_{3n+1}$  ( $n = 3-5$ ) nanosheets were stacked into five layers using the LB process. The colloidal solution was spread on the surface of the DI water in the LB trough, and the movable barrier controlled the surface pressure by compressing the nanosheets on both sides, as illustrated in Supplementary Fig. 3a. The surface pressure increased as the barrier gradually compressed the nanosheets and this tendency is expressed as an isotherm graph (Supplementary Fig. 3b). It was confirmed that all samples showed similar saturation values; therefore, three types of  $\text{Sr}_{1.8}\text{Bi}_{0.2}\text{Na}_{n-3}\text{Nb}_n\text{O}_{3n+1}$  ( $n = 3-5$ ) nanosheets were deposited at  $15 \text{ mN m}^{-1}$  before the saturation value to prevent overlapping areas.

Successful deposition of the nanosheet thin films was confirmed by the UV-visible absorption spectra (Supplementary Fig. 3c). The absorption peaks around 250–300 nm was attributed to the  $\text{Sr}_{1.8}\text{Bi}_{0.2}\text{Na}_{n-3}\text{Nb}_n\text{O}_{3n+1}$  ( $n = 3-5$ ) nanosheets. The continuously increased intensity of the absorption indicates the successful deposition of homologous perovskite nanosheets. After 5 layers of deposition, XRD measurements were performed to confirm that each layer was densely stacked (Fig. 2d). The calculated  $d$  spacing from (002) peak of  $\text{Sr}_{1.8}\text{Bi}_{0.2}\text{Nb}_3\text{O}_{10}$  (3SBNO),  $\text{Sr}_{1.8}\text{Bi}_{0.2}\text{NaNb}_4\text{O}_{13}$  (4SBNNO), and  $\text{Sr}_{1.8}\text{Bi}_{0.2}\text{Na}_2\text{Nb}_5\text{O}_{16}$  (5SBNNO) is 1.6 nm, 2.0 nm, and 2.4 nm, respectively. Therefore, each film was uniformly and densely deposited as a thin film.

The crystal structure and thickness of 5-layer deposited  $\text{Sr}_{1.8}\text{Bi}_{0.2}\text{Na}_{n-3}\text{Nb}_n\text{O}_{3n+1}$  ( $n = 3-5$ ) thin films were investigated using TEM images. Figure 3a shows the top-view and selected area electron diffraction (SAED) patterns of the nanosheets on the holey carbon film-coated TEM grid. The lateral size of the nanosheets was identified in the TEM images as approximately 1  $\mu\text{m}$ . The SAED patterns exhibited the 0.38 nm interplanar distance in the two vertical directions and were indexed to the (100) and (010) planes, indicating the high quality of its single-

crystal nature. Figure 3b shows cross-sectional TEM images of the  $\text{Sr}_{1.8}\text{Bi}_{0.2}\text{Na}_{n-3}\text{Nb}_n\text{O}_{3n+1}$  ( $n = 3-5$ ) thin films on the Nb:STO substrate. All images presented successfully assembled multilayer thin films as lamellar structures with clean interfaces. In addition, we confirm that the thickness of each nanosheet increased with an increasing value of  $n$ , which corresponds to the thickness of the  $\text{NbO}_6$  octahedral unit.

### Electrical properties of nSBNNO ( $n = 3-5$ ) nanosheet film

The electrical properties of  $\text{Sr}_{1.8}\text{Bi}_{0.2}\text{Na}_{n-3}\text{Nb}_n\text{O}_{3n+1}$  ( $n = 3-5$ ) thin films are shown in Fig. 4. To characterize the electrical properties, we deposited 50  $\mu\text{m}$  radius Pt top electrodes on nanosheet films to realize Pt/5-layer  $\text{Sr}_{1.8}\text{Bi}_{0.2}\text{Na}_{n-3}\text{Nb}_n\text{O}_{3n+1}$  ( $n = 3-5$ )/Nb:STO nanocapacitors. First, the leakage current properties of the nanocapacitors were investigated, as shown in Fig. 4a. All 5-layer stacked nanofilms ( $\sim 8 \text{ nm}$  for  $\text{Sr}_{1.8}\text{Bi}_{0.2}\text{Nb}_3\text{O}_{10}$ ,  $\sim 10 \text{ nm}$  for  $\text{Sr}_{1.8}\text{Bi}_{0.2}\text{NaNb}_4\text{O}_{13}$ , and  $\sim 12 \text{ nm}$  for  $\text{Sr}_{1.8}\text{Bi}_{0.2}\text{Na}_2\text{Nb}_5\text{O}_{16}$ ) exhibited highly insulating characteristics below  $\sim 10^{-11} \text{ A}$  at a high breakdown electric field of  $400 \text{ kV cm}^{-1}$ . Above  $400 \text{ kV cm}^{-1}$ , the leakage current gradually increased, and the breakdown voltage increased as the  $n$  of  $\text{NbO}_6$  layers decreased. This tendency can be explained by the quantum-confinement effect<sup>26,34</sup>. It is well known that a large bandgap ensures high breakdown strength<sup>35</sup>. The confinement energy of the conduction band edge decreased with an increase in the  $n$  value, which decreased the bandgap energy. These reduced bandgap energies decrease the breakdown of the electric field.

The dielectric permittivity and dielectric loss of the 5 layers films were investigated. As mentioned in the explanation of Fig. 1d, the dielectric permittivity is apparently related to their structural features. The increased  $\text{NbO}_6$  octahedra leads to higher polarizability and enhanced dielectric permittivity. The dielectric permittivity of the nanosheet films exhibited low dispersion according to the frequency, and the values at 1 kHz increased with an increase in the number of  $n$  layers to 26 ( $\text{Sr}_{1.8}\text{Bi}_{0.2}\text{Nb}_3\text{O}_{10}$ ), 33 ( $\text{Sr}_{1.8}\text{Bi}_{0.2}\text{NaNb}_4\text{O}_{13}$ ), and 62 ( $\text{Sr}_{1.8}\text{Bi}_{0.2}\text{Na}_2\text{Nb}_5\text{O}_{16}$ ) (Fig. 4b), showing the same trend as  $\text{KSr}_{1.8}\text{Bi}_{0.2}\text{Na}_{n-3}\text{Nb}_n\text{O}_{3n+1}$  ( $n = 3-5$ ). In addition, all the thin films showed a low dielectric loss value below 5% in the frequency range of 100 Hz to 1 MHz.

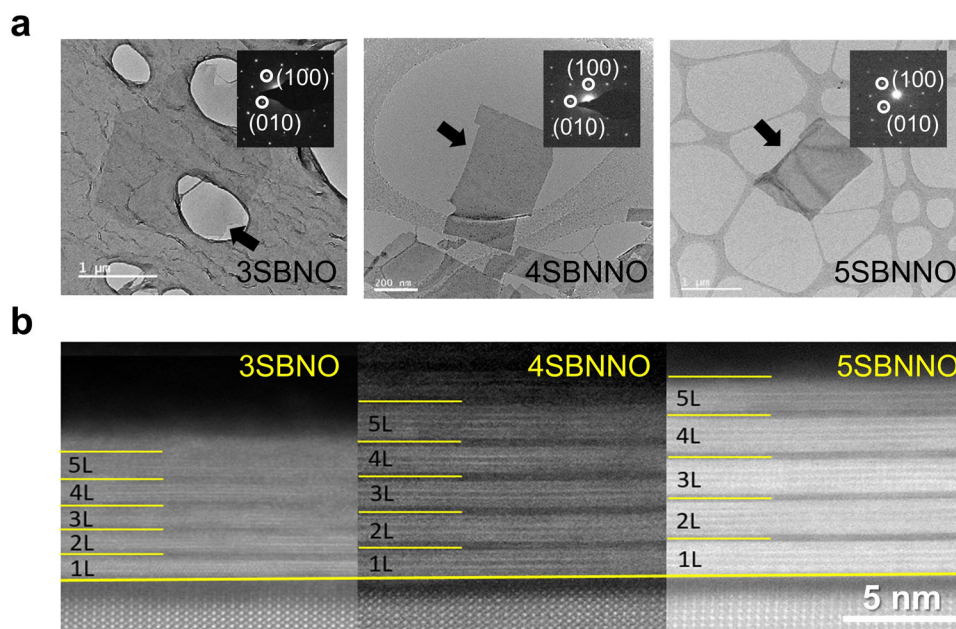


**Fig. 3** TEM analysis of nSBNNO ( $n = 3-5$ ) nanosheet and nanosheet film. **a** Bright-field TEM image and SAED pattern of  $\text{Sr}_{1.8}\text{Bi}_{0.2}\text{Na}_{n-3}\text{Nb}_n\text{O}_{3n+1}$  ( $n = 3-5$ ) (nSBNNO,  $n$  number of  $\text{NbO}_6$  layer) monolayer nanosheet **b** HRTEM image of 5-layer stacked nSBNNO nanosheet films on Nb:STO substrate.

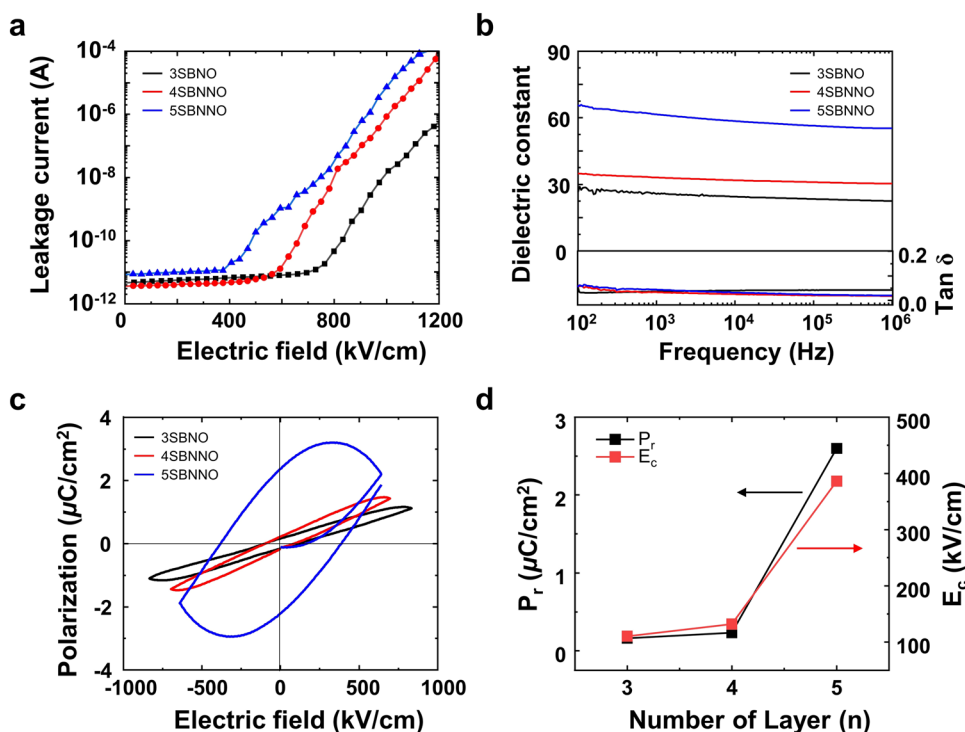


**Fig. 4** Electrical properties of  $n$ SBNNO ( $n = 3\text{--}5$ ) nanosheet film. **a** Leakage current. **b** Dielectric constant and dielectric loss **c** P-E hysteresis loops and **d** Remnant polarization ( $P_r$ ) and coercive field ( $E_c$ ) of the  $\text{Sr}_{1.8}\text{Bi}_{0.2}\text{Na}_{n-3}\text{Nb}_n\text{O}_{3n+1}$  ( $n = 3\text{--}5$ ) ( $n$ SBNNO,  $n$  number of  $\text{NbO}_6$  layer) nanosheet films at room temperature.

Figure 4c shows the P-E characteristics at various applied peak voltages with a field frequency of 1000 Hz, and the remnant polarization ( $P_r$ ) and coercive field ( $E_c$ ) are shown in Fig. 4d. The hysteresis loop indicates the presence of ferroelectricity in 5SBNNO, in contrast to the other samples. The  $\text{Sr}_{1.8}\text{Bi}_{0.2}\text{Nb}_3\text{O}_{10}$  and  $\text{Sr}_{1.8}\text{Bi}_{0.2}\text{NaNb}_4\text{O}_{13}$  nanosheet films exhibited P-E loops close to paraelectricity, and only small spontaneous polarizations were observed. Therefore, it can be concluded that the  $\text{Sr}_{1.8}\text{Bi}_{0.2}\text{Nb}_3\text{O}_{10}$  and  $\text{Sr}_{1.8}\text{Bi}_{0.2}\text{NaNb}_4\text{O}_{13}$  films have paraelectric properties with the  $E_c$  at  $83\text{ kV cm}^{-1}$  ( $P_r$  value was  $0.16\text{ }\mu\text{C cm}^{-2}$ ) and  $115\text{ kV/cm}$  ( $P_r$  value was  $0.23\text{ }\mu\text{C cm}^{-2}$ ), respectively<sup>7,18,36</sup>. In contrast, the  $\text{Sr}_{1.8}\text{Bi}_{0.2}\text{Na}_2\text{Nb}_5\text{O}_{16}$  nanosheet film showed a sophisticated hysteresis response with an  $E_c$  of  $386\text{ kV cm}^{-1}$  and  $P_r$  of  $2.6\text{ }\mu\text{C cm}^{-2}$ . Piezoresponse force microscopy (PFM) is a reliable technique for characterizing the ferroelectric properties of thin films, as all ferroelectrics inherently exhibit piezoelectric behavior<sup>37</sup>. The amplitude of PFM provides information about the local piezoelectric response, indicating its absolute magnitude, while the phase of PFM reveals the polarization direction within each domain<sup>38</sup>. To investigate the effect of ferroelectric in a Pt-coated tip/5SBNNO/Si, we measured ferroelectric switching induced by DC voltage sweep as shown in Supplementary Fig. 4. The local hysteresis loops for PFM were obtained using a commercial atomic force microscopy (AFM) (SPA-300HV, Seiko) with a Pt/Ir coated cantilever. Using a lock-in amplifier (SR830, Stanford Research Systems), the AC probing voltage ( $f = 17\text{ kHz}$ ) was applied in the PFM mode with an amplitude of 1.0 V (peak to peak). Supplementary Figure 4 demonstrates the local PFM hysteresis loop. The coercive voltages of  $-0.6$  and  $0.8\text{ V}$  are derived from the minima of the amplitude loop (bottom panel), which correspond to the voltage at which abrupt phase changes occur (top panel). Therefore, we can confirm the paraelectric-to-ferroelectric transition at the octahedral unit ( $n = 5$ ), which is in good agreement with the previously reported local response<sup>13</sup>.

This ferroelectric transition is known to be caused by the size mismatch of the Sr ( $1.27\text{ \AA}$ )/Na ( $0.98\text{ \AA}$ ) ions along with the  $\text{NbO}_6$

octahedra gradient and the slight Na deficiency in the A-site which leads to the decentralization of the  $\text{Nb}^{5+}$  ions<sup>13</sup>. In addition, the more polarizable Bi ( $1.20\text{ \AA}$ ) ions in Sr/Na sites, which were added to increase the dielectric permittivity, can improve the size mismatch due to their different ionic radii. In addition, the higher distortion of octahedra compared with the parent materials can be caused by surface relaxation during the exfoliation process<sup>13</sup>. Therefore, as the number of  $\text{NbO}_6$  layers increases to  $n = 5$ , sufficient distortion of octahedra is induced in a single-flake nanosheet, which exhibits ferroelectric characteristics.

In summary, we synthesized DJ structure perovskite nanosheets ( $\text{Sr}_{1.8}\text{Bi}_{0.2}\text{Na}_{n-3}\text{Nb}_n\text{O}_{3n+1}$ ,  $n = 3\text{--}5$ ) by exfoliation from the layered perovskite  $\text{KSr}_{1.8}\text{Bi}_{0.2}\text{Na}_{n-3}\text{Nb}_n\text{O}_{3n+1}$  ( $n = 3\text{--}5$ ). As the number of perovskite layers increased, the thickness of the nanosheets also increased. The increased distance along the  $c$ -axis enhanced polarizability in the lattice decreased the optical bandgap and increased the dielectric permittivity. Several 2D materials with ferroelectric characteristics have been proposed, but the P-E characteristics at the device level other than the local area have not been confirmed. Our studies show that the engineering of the  $n$  of octahedral layers with A-site modification is a fascinating strategy to construct ferroelectric materials with increased high- $k$  properties, showing applicability as next-generation two-dimensional devices. For dielectric nanosheets, 3SBNO, have been reported for applied the multilayer films as a gate dielectric in all-2D field effect transistors (FETs)<sup>16</sup>. Additionally, the 5SBNNO presented in this study can also be applied in various application of 2D layered ferroelectric materials including Negative Capacitance Field-Effect Transistors (NC-FETs)<sup>39</sup>, Direct Current Nanogenerator<sup>40</sup>, Nonvolatile Memories and Neuromorphic devices<sup>38</sup>. Therefore, the 2D  $\text{Sr}_{1.8}\text{Bi}_{0.2}\text{Na}_{n-3}\text{Nb}_n\text{O}_{3n+1}$  (octahedral units,  $n = 3\text{--}5$ ) nanosheets possess additional benefits, including the ability to control atomic layer thickness, mechanical flexibility, and the utilization of quantum size effects. These advantages play a significant role in advancing the development of device designs and functionalities in the future.

## METHODS

### Synthesis and analysis of $nK/HSBNO$ ( $n = 3-5$ )

Perovskite  $KSr_{1.8}Bi_{0.2}Na_{n-3}Nb_nO_{3n+1}$  ( $n = 3-5$ ) was synthesized by a conventional solid-state reaction. In a typical synthesis procedure, stoichiometric amounts of  $K_2CO_3$ ,  $SrCO_3$ ,  $Bi_2O_3$ ,  $NaCO_3$ , and  $Nb_2O_5$  (all reagents were purchased from Sigma Aldrich) were mixed for 20 h in a polypropylene jar using zirconia balls. To compensate for the evaporation of  $K_2O$  during the sintering process, an excess of 10 wt%  $K_2CO_3$  was added. The mixed powders were dried at 100 °C for 24 h, calcined at 1100 °C for 10 h, and sintered at 1200 °C ( $n = 3$ ) or 1250 °C ( $n = 4$  and 5) for 10 h in an air atmosphere. The microstructural properties of  $KSr_{1.8}Bi_{0.2}Na_{n-3}Nb_nO_{3n+1}$  ( $n = 3-5$ ) were examined by XRD (DMAX 2500, Rigaku), SEM (Inspect F50, FEI), and Raman spectroscopy (LabRAM ARAMIS IR2, HORIBA JOBIN YVON). The electrical properties were measured using an impedance analyzer (4294 A, Agilent Technologies) in the frequency range of 10 kHz to 10 MHz at room temperature.

The obtained  $KSr_{1.8}Bi_{0.2}Na_{n-3}Nb_nO_{3n+1}$  ( $n = 3-5$ ) sintered powder was acid-treated with a 7 M  $HNO_3$  solution for 7 days to replace interlayer  $K^+$  ions with  $H^+$  ions. The acidic solution was refreshed daily for complete proton replacement. After 7 days, the acid-treated powder was washed several times with deionized (DI) water via centrifugation at 5000 rpm for 10 min. Then,  $HSr_{1.8}Bi_{0.2}Na_{n-3}Nb_nO_{3n+1}$  ( $n = 3-5$ ) powder was dried in an oven at 65 °C for 24 h and added to tetrabutylammonium hydroxide ( $TBA^+OH^-$ ) aqueous solution in a flask. The concentration of  $TBA^+OH^-$  was adjusted to set the molar ratio of  $TBA^+/H^+$  to 1, where  $H^+$  denotes the exchangeable protons in the solid. The mixed solution was shaken by mechanical shaken for 14 days, and  $H^+$  ions in the  $HSr_{1.8}Bi_{0.2}Na_{n-3}Nb_nO_{3n+1}$  ( $n = 3-5$ ) powder were exchanged for bulky  $TBA^+$  ions. The intercalation of bulk  $TBA^+$  ions caused exfoliation of the  $Sr_{1.8}Bi_{0.2}Na_{n-3}Nb_nO_{3n+1}$  ( $n = 3-5$ ) single-crystal nanosheets in the solution.

### Deposition and analysis of $nSBNO$ ( $n = 3-5$ ) nanosheets using LB method

Using the LB method, colloidal nanosheets were deposited on various substrates, including glass, Si wafer, and Nb:STO. The packing density of the  $Sr_{1.8}Bi_{0.2}Na_{n-3}Nb_nO_{3n+1}$  ( $n = 3-5$ ) nanosheets floating at the air/water interface was controlled by adjusting the specific surface pressure via movable barriers. The packed nanosheet was transferred from the water surface to the substrate. This transfer process was repeated several times to achieve the target dielectric film thickness. The nanosheet thin films were irradiated with UV light (UV-ozone cleaning system, Filgen Inc.) using a Xe lamp ( $4\text{ mW cm}^{-2}$ ) for 15 h to photocatalytically decompose the  $TBA^+$  ions<sup>20,41,42</sup>. That is because,  $TBA^+$  still remained on the surface of the nanosheets even after the exfoliation and deposition process is completed<sup>43</sup>. The thickness of the monolayer nanosheet was confirmed using AFM (XE7, Park System). The cross-sectional high-resolution transmission electron microscopy (HRTEM) image of the sample was obtained using a Titan TM 80–300 on a crystal structure of the nanosheets. The dielectric properties were measured using an impedance analyzer (4294 A, Agilent Technology) in the frequency range of 100 Hz to 1 MHz at room temperature, with a platinum top electrode deposited by DC sputtering. Current–voltage ( $I$ – $V$ ) measurements were performed to determine the leakage current characteristics (4155 A, Agilent Technology). Polarization–Electric field ( $P$ – $E$ ) curves were measured using a precise ferroelectric tester system (Precision Premier II, Radiant Technologies) with a microprobe system.

## DATA AVAILABILITY

The data that support the findings of this study are available from the corresponding authors upon request.

Received: 21 February 2023; Accepted: 27 July 2023;

Published online: 11 August 2023

## REFERENCES

- Akinwande, D., Petrone, N. & Hone, J. Two-dimensional flexible nanoelectronics. *Nat. Commun.* **5**, 5678 (2014).
- Zhang, J. L. et al. 2D Phosphorene: epitaxial growth and interface engineering for electronic devices. *Adv. Mater.* **30**, 1802207 (2018).
- Kang, J., Sangwan, V. K., Wood, J. D. & Hersam, M. C. Solution-based processing of monodisperse two-dimensional nanomaterials. *Acc. Chem. Res.* **50**, 943–951 (2017).
- Smith, R. J. et al. Large-scale exfoliation of inorganic layered compounds in aqueous surfactant solutions. *Adv. Mater.* **23**, 3944–3948 (2011).
- Kang, J. et al. Thickness sorting of two-dimensional transition metal dichalcogenides via copolymer-assisted density gradient ultracentrifugation. *Nat. Commun.* **5**, 5478 (2014).
- Kim, Y.-H. et al. Artificial design for new ferroelectrics using nanosheet-architectonics concept. *Nat. nanotech.* **26**, 244001 (2015).
- Osada, M. et al. Robust high- $\kappa$  response in molecularly thin perovskite nanosheets. *ACS Nano* **4**, 5225–5232 (2010).
- Sklute, E. C. et al. Orientation of diamagnetic layered transition metal oxide particles in 1-Tesla magnetic fields. *J. Am. Chem. Soc.* **133**, 1824–1831 (2011).
- Domen, K., Yoshimura, J., Sekine, T., Tanaka, A. & Onishi, T. A novel series of photocatalysts with an ion-exchangeable layered structure of niobate. *Catal. Lett.* **4**, 339–343 (1990).
- Behera, B., Sutar, B. C. & Pradhan, N. R. Recent progress on 2D ferroelectric and multiferroic materials, challenges, and opportunity. *Emergent Mater.* **4**, 847–863 (2021).
- Osada, M. & Sasaki, T. Two-dimensional dielectric nanosheets: novel nanoelectronics from nanocrystal building blocks. *Adv. Mater.* **24**, 210–228 (2012).
- Osada, M. & Sasaki, T. A- and B-site modified perovskite nanosheets and their integrations into high- $k$  dielectric thin films. *Int. J. Appl. Ceram. Technol.* **9**, 29–36 (2012).
- Li, B.-W. et al. Atomic layer engineering of high- $\kappa$  ferroelectricity in 2D perovskites. *J. Am. Chem. Soc.* **139**, 10868–10874 (2017).
- Qi, L., Ruan, S. & Zeng, Y. Review on recent developments in 2D ferroelectrics: theories and applications. *Adv. Mater.* **33**, 2005098 (2021).
- Dai, Y. et al. Ferroelectricity-enhanced Piezo-phototronic effect in 2D V-doped ZnO nanosheets. *Adv. Sci.* **6**, 1900314 (2019).
- Yim, H. et al. Advances in dielectric performance of atomically engineered  $Sr_{1.8}Bi_{0.2}Nb_{3}O_{10}$  perovskite nanosheet thin films. *J. Alloy. Compd.* **925**, 166606 (2022).
- Matsuba, K. et al. Neat monolayer tiling of molecularly thin two-dimensional materials in 1 min. *Sci. Adv.* **3**, e1700414 (2017).
- Osada, M. et al. High- $\kappa$  dielectric nanofilms fabricated from titania nanosheets. *Adv. Mater.* **18**, 1023–1027 (2006).
- Sugimoto, W., Terabayashi, O., Murakami, Y. & Takasu, Y. Electrophoretic deposition of negatively charged tetratitanate nanosheets and transformation into preferentially oriented  $TiO_2(B)$  film. *J. Mater. Chem.* **12**, 3814–3818 (2002).
- Osada, M. et al. Langmuir–Blodgett fabrication of nanosheet-based dielectric films without an interfacial dead layer. *Jpn. J. Appl. Phys.* **47**, 7556–7560 (2008).
- Jacobson, A. J., Johnson, J. W. & Lewandowski, J. T. Interlayer chemistry between thick transition-metal oxide layers: synthesis and intercalation reactions of  $K[Ca_2Na_{n-3}Nb_nO_{3n+1}]$  (3.ltoreq. n .ltoreq. 7). *Inorg. Chem.* **24**, 3727–3729 (1985).
- Li, B.-W. et al. Impact of perovskite layer stacking on dielectric responses in  $KCa_2Na_{n-3}Nb_nO_{3n+1}$  ( $n = 3-6$ ) Dion–Jacobson homologous series. *Appl. Phys. Lett.* **96**, 182903 (2010).
- Vendruscolo, V., Giordano, L., Constantino, V. R. L. & Rodrigues, L. C. V.  $Yb^{3+}/Er^{3+}$  co-doped Dion–Jacobson niobium layered perovskites as NIR-to-green up-conversion materials. *NJC* **44**, 10165–10171 (2020).
- Jehng, J. M. & Wachs, I. E. Structural chemistry and Raman spectra of niobium oxides. *Chem. Mater.* **3**, 100–107 (1991).
- Ge, W. et al. Sol–gel synthesis and dielectric properties of Ruddlesden–Popper phase  $Sr_{n+1}Ti_nO_{3n+1}$  ( $n = 1, 2, 3, \infty$ ). *Ceram. Int* **40**, 1569–1574 (2014).
- Shi, Y. et al. Structure, dielectric and multiferroic properties of three-layered aurivillius  $SrBi_3Nb_2FeO_{12}$  ceramics. *Ceram. Int* **45**, 9283–9287 (2019).
- Sohn, J.-H., Inaguma, Y., Itoh, M. & Nakamura, T. Cooperative interaction of oxygen octahedra for dielectric properties in the perovskite-related layered

- compounds  $\text{Sr}_{n+1}\text{Ti}_n\text{O}_{3n+1}\text{Ca}_{n+1}\text{Ti}_n\text{O}_{3n+1}$  and  $\text{Sr}_{n+1}(\text{Ti}_{0.5}\text{Sn}_{0.5})_n\text{O}_{3n+1}$  ( $n = 1, 2, 3$  and  $\infty$ ). *Mater. Sci. Eng. B* **41**, 50–54 (1996).
28. Toda, K. et al. Characterization of potassium niobate produced by self-assembled nanosheet from aqueous solution. *Jpn J. Appl Phys.* **41**, 7021–7024 (2002).
  29. Kłodzińska, E. et al. Effect of zeta potential value on bacterial behavior during electrophoretic separation. *Electrophoresis* **31**, 1590–1596 (2010).
  30. Khan, M. S. et al. Rational assembly of two-dimensional perovskite nanosheets as building blocks for new ferroelectrics. *ACS Appl Mater. Interfaces* **13**, 1783–1790 (2021).
  31. Asaki, S. et al. Ferroelectricity of Dion–Jacobson layered perovskites  $\text{CsNdNb}_2\text{O}_7$  and  $\text{RbNdNb}_2\text{O}_7$ . *Jpn J. Appl Phys.* **59**, SPPC04 (2020).
  32. Pan, B. et al. Electrostatic self-assembly behaviour of exfoliated  $\text{Sr}_2\text{Nb}_3\text{O}_{10}$ –nanosheets and cobalt porphyrins: exploration of non-noble electro-catalysts towards hydrazine hydrate oxidation. *J. Mater. Sci.* **53**, 6494–6504 (2018).
  33. Guo, W., Yang, Z., Dang, J. & Wang, M. Progress and perspective in Dion–Jacobson phase 2D layered perovskite optoelectronic applications. *Nano Energy* **86**, 106129 (2021).
  34. Suzuki, K. & Kijima, K. Optical band gap of barium titanate nanoparticles prepared by RF-plasma chemical vapor deposition. *Jpn J. Appl Phys.* **44**, 2081 (2005).
  35. Alamri, A. et al. High dielectric constant and high breakdown strength polyimide via tin complexation of the polyamide acid precursor. *RSC Adv.* **12**, 9095–9100 (2022).
  36. Im, M., Lee, W.-H., Kweon, S.-H. & Nahm, S. New lead-free piezoelectric thin film fabricated using metal-oxide nanosheets at low temperature. *Ceram. Int* **45**, 21773–21780 (2019).
  37. Guan, Z. et al. Recent progress in two-dimensional ferroelectric materials. *Adv. Electron Mater.* **6**, 1900818 (2020).
  38. Jin, T. et al. Ferroelectrics-integrated two-dimensional devices toward next-generation electronics. *ACS Nano* **16**, 13595–13611 (2022).
  39. Zhai, Y., Feng, Z., Zhou, Y. & Han, S.-T. Energy-efficient transistors: suppressing the subthreshold swing below the physical limit. *Mater. Horiz.* **8**, 1601–1617 (2021).
  40. Gupta, M. K., Lee, J.-H., Lee, K. Y. & Kim, S.-W. Two-dimensional vanadium-doped  $\text{ZnO}$  nanosheet-based flexible direct current nanogenerator. *ACS Nano* **7**, 8932–8939 (2013).
  41. Sasaki, T. et al. Titania nanostructured films derived from a titania nanosheet/polycation multilayer assembly via heat treatment and UV irradiation. *Chem. Mater.* **14**, 3524–3530 (2002).
  42. Yano, H. et al. Construction of multilayer films and superlattice- and mosaic-like heterostructures of 2D metal oxide nanosheets via a facile spin-coating process. *ACS Appl Mater. Interfaces* **13**, 43258–43265 (2021).
  43. Lee, Y.-S., Yim, H., Yoo, S.-Y., Ju, B.-K. & Choi, J.-W. Dielectric properties of single crystal  $\text{Sr}_2\text{Nb}_3\text{O}_{10}$  dielectric nanosheet thin films by electrophoretic deposition (EPD) and post deposition treatments. *J. Alloy. Compd.* **711**, 51–57 (2017).

## ACKNOWLEDGEMENTS

This research was supported by the Korea Institute of Science and Technology Future Resource Program (2E32491), the National Research Foundation of Korea (NRF) grant funded by the Korean government (No. 2021R1A2C2010695), Green New Deal 100

Promising Company 100 R&D Program (2MRC190) funded by the Ministry of SMEs and Stratups (MSS, Korea), Korea Basic Science Institute (National research Facilities and Equipment Center) grant funded by the Ministry of Education (Grant No. 2022R1A6C101A754) and National R&D Programs (No. 2022R1A2C3004135) through the National Research Foundation of Korea (NRF) funded by Ministry of Science.

## AUTHOR CONTRIBUTIONS

S.-Y.Y. and H.Y. synthesized nanosheets and obtained the characteristic of nanosheets thin films including XRD, AFM, and TEM. S.-Y.Y. investigated the electrical properties of nanosheets thin film. C.Y. performed the PFM experiments. A.R. carried out the deposition of Pt thin film as top electrode using DC sputtering. H.Y. wrote the manuscript with the help of A.R. J.-W.C., B.H.P. and S.N. conceptualized the work, and all the authors contributed to the final version of the manuscript.

## COMPETING INTERESTS

The authors declare no competing interests.

## ADDITIONAL INFORMATION

**Supplementary information** The online version contains supplementary material available at <https://doi.org/10.1038/s41699-023-00418-9>.

**Correspondence** and requests for materials should be addressed to Ji-Won Choi.

**Reprints and permission information** is available at <http://www.nature.com/reprints>

**Publisher's note** Springer Nature remains neutral with regard to jurisdictional claims in published maps and institutional affiliations.



**Open Access** This article is licensed under a Creative Commons Attribution 4.0 International License, which permits use, sharing, adaptation, distribution and reproduction in any medium or format, as long as you give appropriate credit to the original author(s) and the source, provide a link to the Creative Commons license, and indicate if changes were made. The images or other third party material in this article are included in the article's Creative Commons license, unless indicated otherwise in a credit line to the material. If material is not included in the article's Creative Commons license and your intended use is not permitted by statutory regulation or exceeds the permitted use, you will need to obtain permission directly from the copyright holder. To view a copy of this license, visit <http://creativecommons.org/licenses/by/4.0/>.

© The Author(s) 2023